Marine and Petroleum Geology 147 (2023) 105980

Contents lists available at ScienceDirect

Marine and Petroleum Geology

journal homepage: www.elsevier.com/locate/marpetgeo

# Imaging of small-scale faults in seismic reflection data: Insights from seismic modelling of faults in outcrop

Vilde Dimmen *, Atle Rotevatn, Isabelle Lecomte

*Department of Earth Science, University of Bergen, PO Box 7800, 5020 Bergen, Norway*

ARTICLE INFO

*Keywords:*
seismic Imaging
Sub-seismic
Carbonates
Normal faults
Ormsby wavelet
PSDM

ABSTRACT

Faults with throws that fall below vertical seismic resolution are challenging to identify in reflection seismic datasets. Nevertheless, such small-scale faults may still affect the seismic images, and in this study, we build seismic models of outcrop analogues to investigate *how*. Using photogrammetry from faults affecting Oligocene to Miocene carbonate rocks in Malta, we build a series of geological models from which synthetic seismic images are produced. The resulting seismic images are analysed to elucidate the effects of varying geologic input, signal properties and introduction of noise, and compared to real seismic data from the SW Barents Sea, offshore Norway. Our results suggest that at signal peak frequencies of 30 Hz and higher, using the classic Ricker wavelet type and without introducing noise, graben forming faults with a combined displacement down to ~5 m affect the seismic image by slight downwarping of reflections, whereas single faults with displacement down to ~10 m show detectable non-discrete reflection offsets in form of a monoclinal geometry at signal peak frequencies at 60 Hz. Using an Ormsby wavelet, we get seismic images with a quality that lie in between that of the 30 Hz and 60 Hz Ricker, even though the peak frequency is lower. The identified structures can also be seen when noise is included, although the reflections are more irregular and harder to detect. This suggests that under relatively noise-free conditions in high-quality reflection seismic datasets, lower-throw faults (as low as 5 m in this study) that do not induce discrete reflection offsets in seismic images may still produce reflection distortions. Additionally, seismic modelling using the Ormsby wavelet, and its effect on the seismic image, is lacking in literature as of today. We suggest that the results and examples shown in this study may be used to geologically inform fault interpretations in real seismic datasets and may form an empirical basis for geologically concept-driven fault interpretation strategies.

## 1. Introduction

Faults of all scales play a crucial role for accommodating deformation and fluid flow within the upper crust (Caine and Forster, 1999; Faulkner et al., 2010). Understanding the role of faults in for example exploration for, and exploitation of, petroleum, mining, and groundwater resources, are of great economic significance since faults often control fluid migration, induce reservoir/aquifer compartmentalisation, and determine the location of ore deposits (e.g. Aydin, 2000; Gartrell et al., 2004; Bense and Person, 2006; Rotevatn and Fossen, 2011; Beukes et al., 2013; Dimmen et al., 2020; Bradaric et al., 2022). Fault-controlled fluid flow is also important from an environmental/hazards perspective, and relevant for example in subsurface carbon storage, contaminant transport and the storage of nuclear waste (Talwani, 1999; Moussa and El Arabi, 2003; Shipton et al., 2005; Yoshida et al., 2008; Krawczyk et al., 2015). For most of the above applications, fault detection and mapping in the subsurface is key to understanding fault geometry, dimensions, distribution, and properties.

The detection of faults in the subsurface often depends on the use of reflection seismic data, coming with several limitations. The vertical resolution i.e., of seismic datasets constrains our ability to identify geological layers, the minimum vertical distance between two features (reflectors) that are possible to define separately rather than as one. Vertical seismic resolution is controlled by the wavelength of the seismic signal; the Rayleigh criterion states that the vertical resolution limit is a quarter-wavelength (e.g. Knapp, 1990). For modern, commercial, high-quality 3D seismic data sets this may translate to a vertical resolvability of 10–30 m at best. This defines an approximate lower practical constraint on seismically resolvable fault offsets. The relatively high-angle nature of most extensional faults means that the seismic

* Corresponding author. (V. Dimmen).
*E-mail address:* vilde.dimmen@uib.no (V. Dimmen).

https://doi.org/10.1016/j.marpetgeo.2022.105980
Received 3 March 2022; Received in revised form 13 September 2022; Accepted 16 October 2022
Available online 22 October 2022

waves will not hit and illuminate the actual fault surface, except when using very wide offsets. Therefore, most faults are so-called non-illuminated faults, and are detected from breaks in reflection continuity rather than by discrete imaging of the fault itself. In addition, limited lateral resolution blurs the seismic images (Fresnel zone effect) and may induce lateral smearing across non-illuminated fault zones; this can prevent accurate dip estimations, even if 3D migration reduces the Fresnel-zone down to half-wavelength (Simm and Bacon, 2014). Also, faults dipping at an angle greater than ~40–50° are generally too steep to be illuminated and imaged in reflection seismic data (Simm and Bacon, 2014; Chen and Huang, 2015), and their presence is therefore generally inferred by the identification of discontinuous reflections of the displaced geological strata. There are also other limitations that come into effect in the imaging of subsurface geology with reflection seismic data, such as noise and decrease of signal/image quality with depth due to geometrical spreading, attenuation of seismic energy with the high frequencies being especially absorbed, and scattering of the seismic signal by e.g. faults and fault-block crests (Simm and Bacon, 2014; Lecomte et al., 2015).

Small-scale faults and other types of fractures that fall below seismic resolution are very important, since i) fault/fracture sizes in nature follow a power-law distribution, which means there are infinitely greater numbers of smaller (sub-seismic) structures than greater (seismically resolvable) structures in any rock deformed in a brittle manner (e.g. Hatton et al., 1994; Vermilye and Scholz, 1995; Renshaw and Park, 1997); ii) sub-seismic structures may accommodate significant crustal strains; for example, Walsh et al. (1991) suggest that seismic-based summations of fault throws may underestimate regional extension by up to 40% (depending on the seismic resolution of the datasets used), due to sub-seismic strains; and iii) sub-seismic structures are critical for controlling permeability and fluid flow patterns in the sub-surface (e.g. Damsleth et al., 1998; Walsh et al., 1998; Mitchell and Faulkner, 2012), because they provide structural connectivity between larger seismically mappable structures (e.g. Gartrell et al., 2004; Dimmen et al., 2017; Sanderson and Nixon, 2018). Hence, it is important to be aware of these structures and get the best possible understanding of them.

Although structural features that fall below seismic resolution cannot be directly resolved, they may still affect the seismic image. To the best of our knowledge, no previous seismic modelling studies have attempted to investigate the effect of such structures on seismic images. Motivated by this, we explore the effects that sub-seismic faults may have on a seismic image, to better understand how some sub-seismic structures may be inferred.

In this paper, we study carbonate-hosted normal faults from the west coast of Malta with displacements of 20 m and below and conduct seismic modelling to investigate their effect on seismic images. As such, the studied faults fall approximately at or below the limits of what is practically resolvable in modern, commercial reflection seismic data. The key question we ask is "*how do faults that are borderline seismically resolvable, or that fall below seismic resolution, affect seismic images?*". Secondly, we look into how structural complexity associated with such small-scale faults affect a seismic image, and whether the seismic image of simpler fault geometries (e.g., a single fault strand) differ from seismic images of more complex fault geometries (in this case a fault comprised of two fault strands forming a fault-bounded lens). In addition to looking into how the structural geometries affect the seismic image, we also investigate the effect of various signal properties on the seismic images by varying wavelet type and wave frequencies, and by varying lateral resolution. We also look at the effect of introducing noise, which is generally present in real seismic data, and, finally, compare our synthetic images with real, high-quality seismic images from a carbonate-dominated succession in the Barents Sea, offshore Norway.

## 2. Geologic framework of the faults used in the seismic models

The normal faults that form the basis for the seismic models herein are hosted in Late Oligocene to Early Miocene limestones in western Malta (Fig. 1 a). The Maltese islands are situated on the NE shoulder of the Pantelleria rift system, which formed in Late Miocene-Early Pliocene as a result of roll-back and eastward migration of the Apennine-Maghrebian subduction zone (Dart et al., 1993; Gueguen et al., 1998; Cavazza and Wezel, 2003). The rifting event caused the formation of ENE-WSW trending horst and graben structures that now dominate the Maltese archipelago (Bonson et al., 2007; Putz-Perrier and Sanderson, 2010). The studied areas are located in cliff sections at Ras-Ir-Raheb, immediately south of Fomm-Ir-Rih bay and approximately 500 m into the footwall of the regionally significant Victoria Lines Fault (~90 m displacement; Fig. 1 a). The cliff sections, which are easily accessible, host a range of smaller-scale normal faults with displacements in the range of <1–20 m (Michie et al., 2014; Dimmen, 2016; Nixon et al., 2020). The faults are hosted within a shallow-marine carbonate succession that comprises the middle part of the Oligocene-Quaternary stratigraphy of the Maltese archipelago (Fig. 1 b).

The regional stratigraphy of Malta is divided into pre-, syn-, and post-rift successions, with respect to the Pantelleria rifting event (e.g. Pedley et al., 1976; Dart et al., 1993). The pre-rift succession includes platform carbonates comprising the Lower Coralline Limestone Formation of Late Oligocene age and the pelagic Early Miocene Lower Globigerina Limestone Member of the Globigerina Limestone Formation (Pedley et al., 1976). The syn-rift stage (21–1.5 Ma) is represented by i) fine-grained foraminiferal limestones of the Middle and Upper Globigeringa Limestone members, followed by ii) pelagic marls and clays constituting the Blue Clay Formation, iii) a marly glauconite lag named the Greensand Formation (however not present in our study area) and iv) shallow-water limestones and marls of the Upper Coralline Limestone Formation (Pedley et al., 1976; Dart et al., 1993). The post-rift sequence consists predominantly of Quaternary deposits, and includes terrestrial, pelagic and hemipelagic sediments (Pedley et al., 1976; Jongsma et al., 1985; Dart et al., 1993). The studied faults are mainly hosted in the Lower Coralline Limestone Formation and Globigerina Limestone Formation, although some continue up-dip into overlying strata.

## 3. Methodology

### 3.1. Collection and processing of outcrop imagery and observations

Faults were mapped along the studied cliff sections at two localities at Ras-Ir-Raheb (Fig. 1 a), and map-view and cliff-section imagery with 60–80% overlap was collected using a drone (DJI Mavic Pro). The imagery was used to create photo panels and 3D photogrammetric models (Fig. 2 a) through AgiSoft PhotoScan Professional (v. 1.3.4). Structures and stratigraphic boundaries were then digitized/interpreted on the 3D photogrammetric models with help from the data collected in the field using the software LIME (Buckley et al., 2019). The 3D interpretations were then projected onto a vertical 2D panel (a 2D surface), that formed the basis for our 2D geological models (Fig. 2 b). In areas where erosion and vegetation obscure continuous exposure, faults and stratigraphic boundaries were extrapolated from exposed areas. The 2D geological models were then converted to grayscale and populated with elastic properties using a Matlab script. The script generates the input files containing the elastic properties needed for the seismic modelling described below.

### 3.2. Seismic modelling methodology

Seismic modelling can be a cost-efficient and effective way of improving interpretation of seismic data while helping better understanding the seismic response of the subsurface (e.g. Botter et al., 2016; Eide et al., 2017; Grippa et al., 2019; Faleide et al., 2021). The methodology used in this paper will be briefly described here; for a more detailed account of the method and workflow, see Lecomte (2008) and Lecomte et al. (2015).

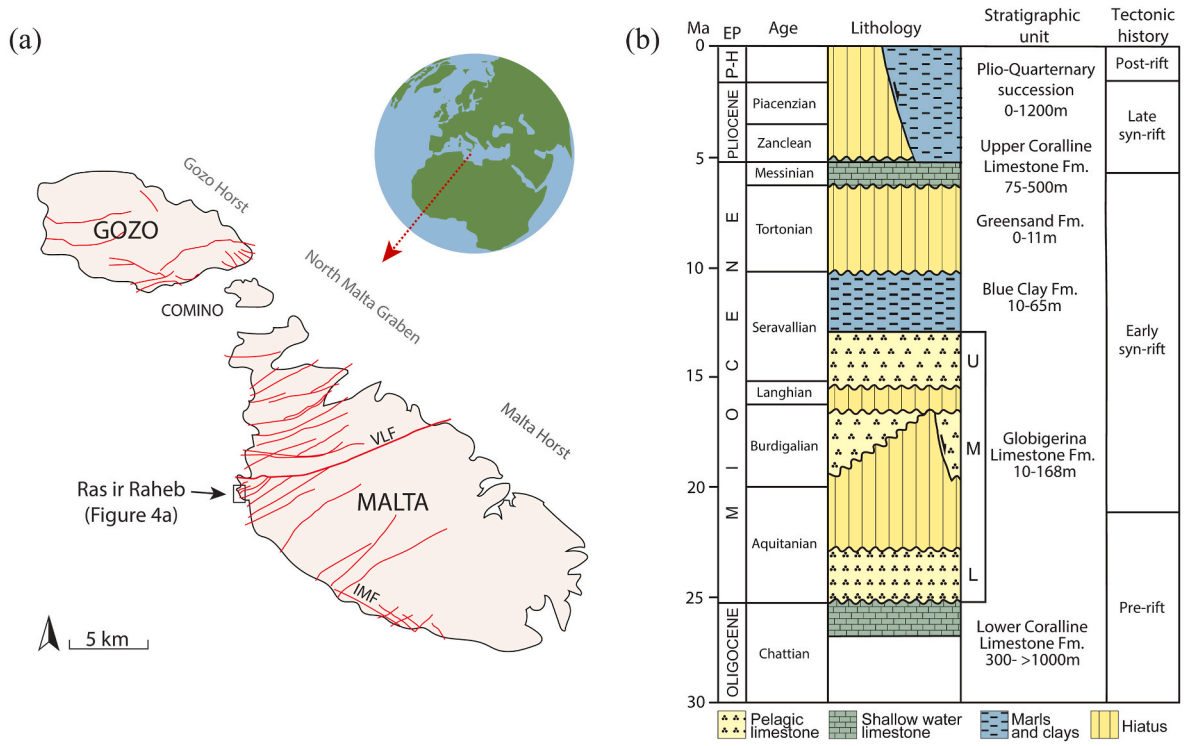


**Fig. 1.** a) The Maltese Islands in the Mediterranean Sea, showing the study area of Ras-Ir-Raheb on the west coast of Malta, just south of the Victoria Lines Fault (VLF). (After Pedley et al., 1976; Michie et al., 2014; Dimmen et al., 2017). b) General stratigraphy of the Maltese Islands (From Dart et al. (1993) and Bonson et al. (2007)).

We use a 2D convolution approach because the standard and most-applied 1D convolution method (either implemented as purely 1D for simulating well ties, or 'pseudo-2D' using serial-1D convolution when modelling seismic sections) does not properly account for laterally varying structures, limited illumination and lateral resolution (Lecomte et al., 2016; Jafarian et al., 2018; Lubrano-Lavadera et al., 2018). The convolution method used here is also available in 3D; however, the 2D version is preferred since it is ideal for representing the cliff sections studied herein, and since 2D representation involves fewer assumptions and extrapolations of fault geometries.

The 2D convolution method is originally a ray-based approach, which generate one (or several) point-spread function (PSF, see Fig. 2 c/d) as the convolution kernel which is applied to an input reflectivity model (Fig. 2 c) to create a synthetic seismic image (Fig. 2 d). Compared to the 1D convolution method, the 2D method produces a more realistic seismic image, simulating pre-stack depth-migrated (PSDM) seismic sections (Lecomte et al., 2016; Eide et al., 2017). In lack of a specific overburden model and survey geometry, especially when studying outcrops, the PSF can be simply created from a few key parameters (Lecomte et al., 2016), i.e. an angle of illumination, an incident angle, an average velocity for the targeted zone (here, the outcrop), and a wavelet (as in 1D convolution). For this study, we keep the incident angle at 0°, while the maximum illumination dip angle is set to 45°, as seismic surveys typically illuminate reflectors dipping up to 40°–50° (Eide et al., 2017; Wrona et al., 2020). Higher angle of illumination generally gives a better image, and an illumination angle of 90° would theoretically give 'perfect illumination'. We used three different wavelets, described more thoroughly in the following sub-chapter.

The models also need to be given realistic petrophysical properties; the P- and S-wave velocities ($V_p$ and $V_s$, respectively) used to populate the models are based on $V_p/V_s$ values from literature (see Table 1 and references therein) and adjusted for variation based on actual $V_p$ and $V_s$ from soft and hard carbonate rocks in the Barents Sea (J. Herredsvela, pers. comm., 2018). Petrophysical properties were added to the models using a Matlab script, and each geological formation was given a couple of values in order to create some internal variation.

We do not include an overburden model since the effect of overburden is factored into our selection of petrophysical properties that reflect a burial depth of ~2 km. Densities were calculated using the original Gardner relation which describes the relationship between density and $V_p$ (Gardner et al., 1974).

$$\rho = aVp^{1/4} \quad (1)$$

where ρ is the density (g/cm$^3$), a = 0.31 and Vp is in km/s (Gardner et al., 1974; Dey and Stewart, 1997).

### 3.3. Varying signal properties and noise

#### 3.3.1. Wavelet types

We ran each model with two different wavelet types: the Ricker and Ormsby wavelet (Ryan, 1994). The Ricker wavelet was chosen because it is frequently used in seismic modelling (e.g. Botter et al., 2016; Eide et al., 2017; Lubrano-Lavadera et al., 2018; Wrona et al., 2020) due to its simple relation between peak frequency and wavelet breadth, while the Ormsby wavelet is made to mimic a more realistic wavelet as extracted from the real seismic data we will use to compare our results with. The Ricker wavelet was run using two different peak frequencies: a 30 Hz peak was chosen to emulate relatively low-resolution seismic data, while a 60 Hz peak was used to emulate high-resolution seismic data. The synthetic Ormsby wavelet was created in Petrel using the low-cut, low-pass, high-pass and high-cut frequencies of 1-3-15-110 Hz, respectively.

Fig. 3 shows the three wavelets (a) and their frequency range (b). The Ormsby wavelet has much smaller side lobes compared to both the 30- and 60 Hz Ricker wavelets, while having a main-peak width (here defined between the first zero crossings) closer to the one of the 30 Hz Ricker rather than that of the 60 Hz Ricker (Fig. 3 a). Looking at the frequency contents (Fig. 3 b), the dominant frequency of the 30 Hz

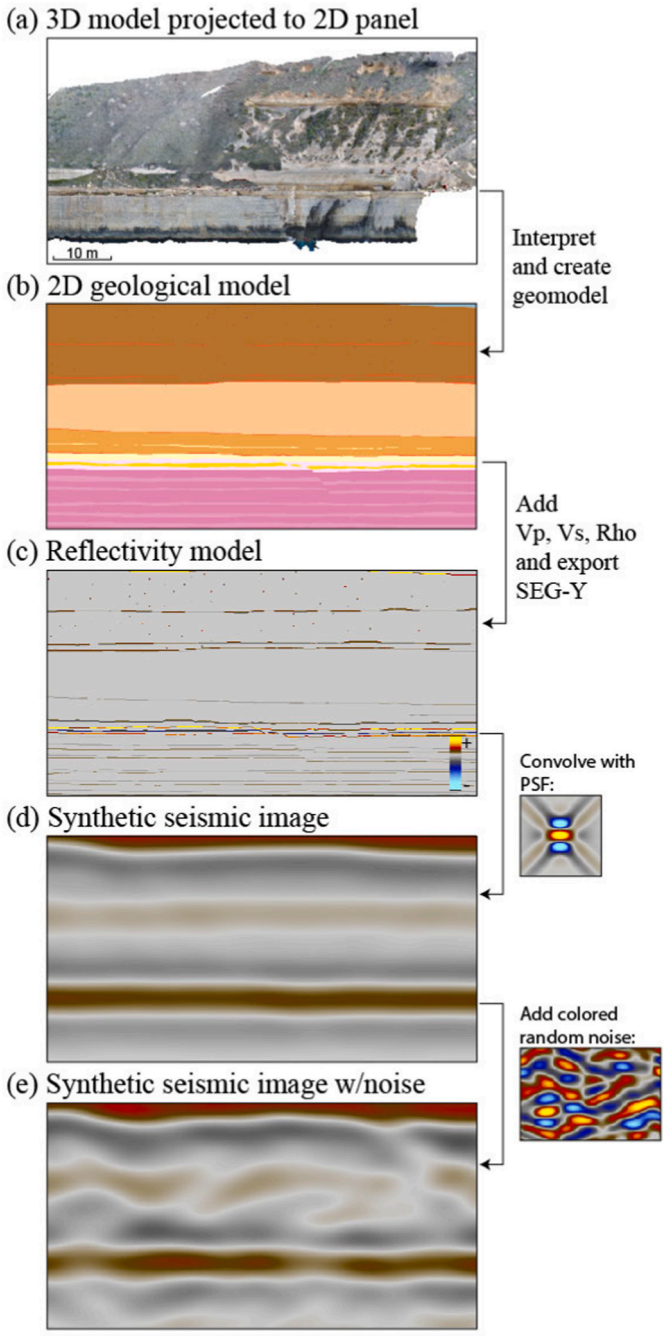


**Fig. 2.** a) A 3D outcrop model as portrayed in AgiSoft PhotoScan Professional. The model is interpreted and extrapolated to create the 2D geological model in (b). The Geological model is exported in gray scale and populated with elastic properties using a matlab-script that provides SEG-Y files for input to SeisRoX. c) A reflectivity model is created in SeisRoX and convolved with a point spread function (PSF) to create the synthetic seismic image as seen in d). e) For more realism, the seismic is combined with random noise.

Ricker (i.e., 30 Hz per definition in such idealized Ricker wavelet) is actually higher than the one of the Ormsby (15 Hz), but its bandwidth is considerably smaller than those of the two other wavelets. Shallow targets generally have higher bandwidth than deeper targets, and higher bandwidth essentially means greater power of resolution (Simm and Bacon, 2014). The peak frequency of the Ormsby wavelet is closer to the 30 Hz Ricker than the 60 Hz one, though its lack of significant side lobes – due to the progressive dimming of the high frequencies - makes it a better wavelet in terms of resolution.

**Table 1**
Petrophysical properties given to geological 2D models through a MATLAB-script creating SEG-Y files.

| Formation | $V_p$ (km/s) | $V_s$ (km/s) | Density (kg/m$^3$) | Reference |
|---|---|---|---|---|
| Upper Coralline Limestone Fm. | 4.80–5.90 | 2.53–3.12 | 2.58–2.72 | Pickett, 1963; Anselmetti and Eberli, 1993 |
| Blue Clay Fm. | 1.90–2.50 | 1.00–1.32 | 2.05–2.19 | Pickett, 1963; Castagna et al., 1993Castagna et al., 1993 |
| Upper Globigerina Limestone Mbr. | 4.00–4.50 | 2.11–2.37 | 2.47 | Pickett, 1963 |
| Middle Globigerina Limestone Mbr. | 4.20–4.35 | 2.21–2.29 | 2.52 | Pickett, 1963; Healy et al., 2015 |
| Lower Globigerina Limestone Mbr. | 3.80–4.50 | 2.00–2.37 | 2.43 | Pickett, 1963,; Healy et al., 2015 |
| Lower Coralline Limestone Fm. | 5.50–5.80 | 2.89–3.05 | 2.67–2.71 | Pickett, 1963; Healy et al., 2015 |

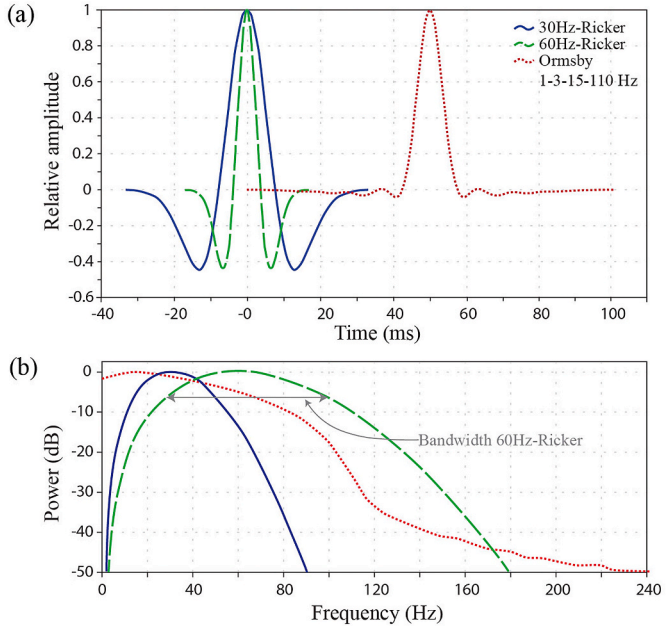


**Fig. 3.** a) Shape of the three wavelets used for this study. The Ormsby wavelet clearly has much smaller side lobes than the Ricker wavelets. b) corresponding frequency spectrum for the three wavelets. The 30 Hz-Ricker wavelet has a bandwidth of ~15–50 Hz, the 60 Hz-Ricker wavelet ~30–100 Hz, while the Ormsby wavelet spans ~0–70 Hz.

### 3.3.2. *Adding random noise*

The 2D PSF-based convolution method used to create the seismic does not add any noise except for the imaging noise from side lobes of the PSF. In the case of a known overburden, the PSF could have been efficiently estimated by ray-based approaches to further constrain a more realistic illumination pattern, this PSF thus possibly showing other sources of imaging noise due to, e.g., too coarse sampling of the survey or irregular illumination due to the wave propagation through the overburden. However, we restrained the study to a more “ideal” case, with a PSF simply constrained by a few key parameters as described above. The synthetic seismic images that are produced are therefore

very 'clean', yet reproducing a complete resolution pattern, both vertically and laterally, and with the (realistic) lack of imaging of steep dips. Nevertheless, in real seismic data, the signal-to-noise ratio is one of the parameters affecting the detectability of structures (Simm and Bacon, 2014; Lubrano-Lavadera et al., 2018) and in order to detect reflections from geological structures in the seismic, the amplitude needs to be significantly higher than that of the seismic noise (Eide et al., 2017).

We therefore added random noise to the modelling and considered a signal-to-noise ratio of 4 (20% noise) to emulate such detectability issues. This was chosen based on the results from Andersen (2020), who found that carbonate hosted faults may be visible in seismic with ≥25% noise, but hardly detectable when the noise is increased to 50%. The noise was created as an additional seismic image by convolving random (white) noise, given as an input reflectivity grid, with the PSF of the associated synthetic seismic, thus colouring the random noise with the same frequency and wavenumber range as the modelled seismic sections (PSDM-coloured noise). The PSF-convolved random noise was then added to the seismic images of the outcrop models as an individual step (Fig. 2 d/e). All synthetic seismic images are presented *with* and *without* noise in the results section. All seismic (and noise) was also amplitude-calibrated, so that a peak of a certain strength in reflectivity would correspond to a peak of the same strength in the seismic images. The seismic are displayed with normal polarity, whereby an increase in acoustic impedance is represented by a peak (red), and a decrease by a trough (blue).

## 4. Experimental design

The models used herein are based on two main outcrops in the study area (Fig. 4) From each of the outcrops, we created a modelling series consisting of three different geological models, giving a total of six cases, covering fault offsets from ~1 to 20 m (Fig. 5). Variation of wavelet type and frequency, and addition or absence of noise in the six models lead to a total of 36 seismic images for discussion. As previously mentioned, the results will be compared to real, high-quality seismic images (TopSeis) from a carbonate-dominated succession in the SW Barents Sea, offshore Norway, of Carboniferous to Triassic age. The area we will be looking at lies at approximately 2000 m depth, in the proximity of a km-scale rotated fault block with several horst-and-graben forming faults in the overburden.

### 4.1. Outcrop 1; model series 1

The area where the first outcrop is located sits approximately 500 m into the footwall of the larger (displacement D = 90 m) Victoria Lines Fault at Ras-Ir-Raheb (Fig. 4 a). The outcrop displays several smaller faults with offsets <1 m in the fine grained, homogenous Middle and Lower Globigerina Limestone Members (Fig. 4 b). The faults cut through the boundary between the two members, which is marked by a layer of phosphoritic conglomerate. The outcrop selected for modelling from this area is a compound graben structure with a combined offset of c. 1 m, distributed across several faults. The models are extended to include significantly more of the outcrop than the compound graben itself; the models are therefore 300 m wide and 200 m tall, extending approximately 30 m into the Upper Coralline Formation at the top and the Lower Coralline Formation at the bottom (Fig. 4 c).

Three models were created based on the compound graben structure from the first outcrop (Fig. 5). First, a fault-free reference model with sub-horizontal bedding (Model 1.1) was created to serve as baseline for comparison with the faulted models. The actual fault geometries recorded at the outcrop are represented in Model 1.2, whereas in Model 1.3 the combined offsets were exaggerated to 5 m. Model 1.3 is otherwise identical to Model 1.1 and 1.2.

### 4.2. Outcrop 2; model series 2

The area where the second outcrop is situated sits ~700 m south of Outcrop 1 and ~1.2 km into the footwall of the Victoria Lines Fault (Fig. 4 a). The outcrop of interest features a fault with a displacement of approximately 11 m (Fig. 4 b). The fault is comprised of two strands and dissects the uppermost part of the Lower Coralline Limestone and continues down-dip below sea level. Up-dip, it extends through the Lower-, Middle- and Upper Globigerina Limestone members, and into the Blue Clay Formation. The fault does not extend further up-dip into the Upper Coralline Formation and, although the tip itself is not exposed, we infer that the fault tips out below the base of this formation. The two fault strands bound a lens-shaped geometry, where the total throw of the fault is shared between the two strands (Haines et al., 2016).

Three different models were created with the aim of investigating the effects of the fault itself and the lens-shaped geometry on seismic images (Fig. 5). To do this, we created a reference model where the fault

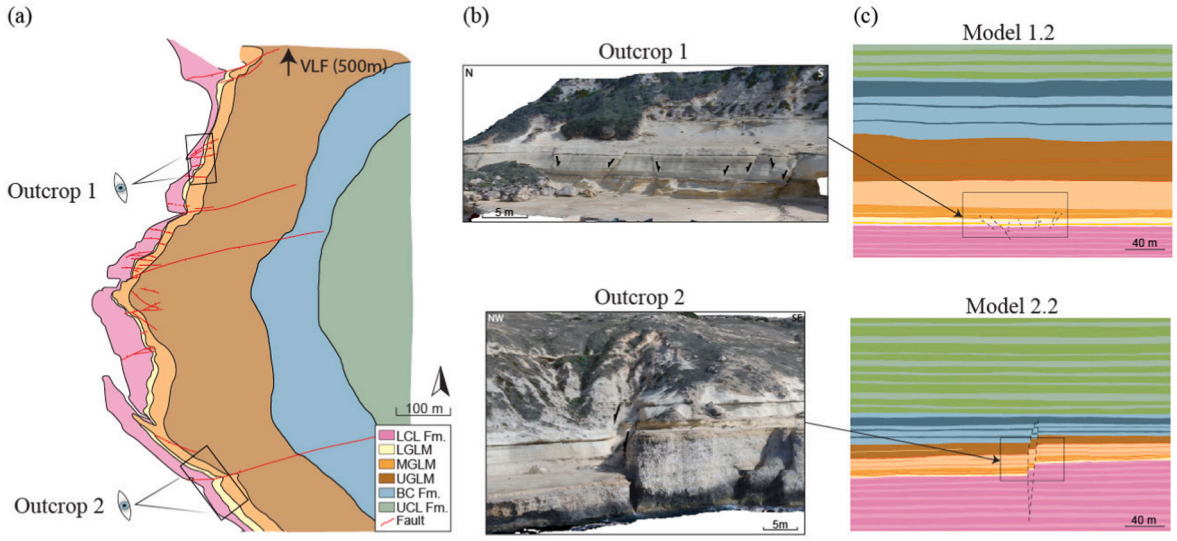


**Fig. 4.** a) Overview of Ras-Ir-Raheb and the location of the two outcrops, outcrop 1 in the northern part and outcrop 2 in the southern part of the map. LCL = Lower Coralline Limestone, LGLM = Lower Globigerina Limestone Member, MGLM = Middle Globigerina Limestone Member, UGLM= Upper Globigerina Limestone Member, BC = Blue Clay, UCL= Upper Coralline Limestone b) 3D models of the selected outcrops and their position in the finished geological models in c). (For interpretation of the references to colour in this figure legend, the reader is referred to the Web version of this article.)

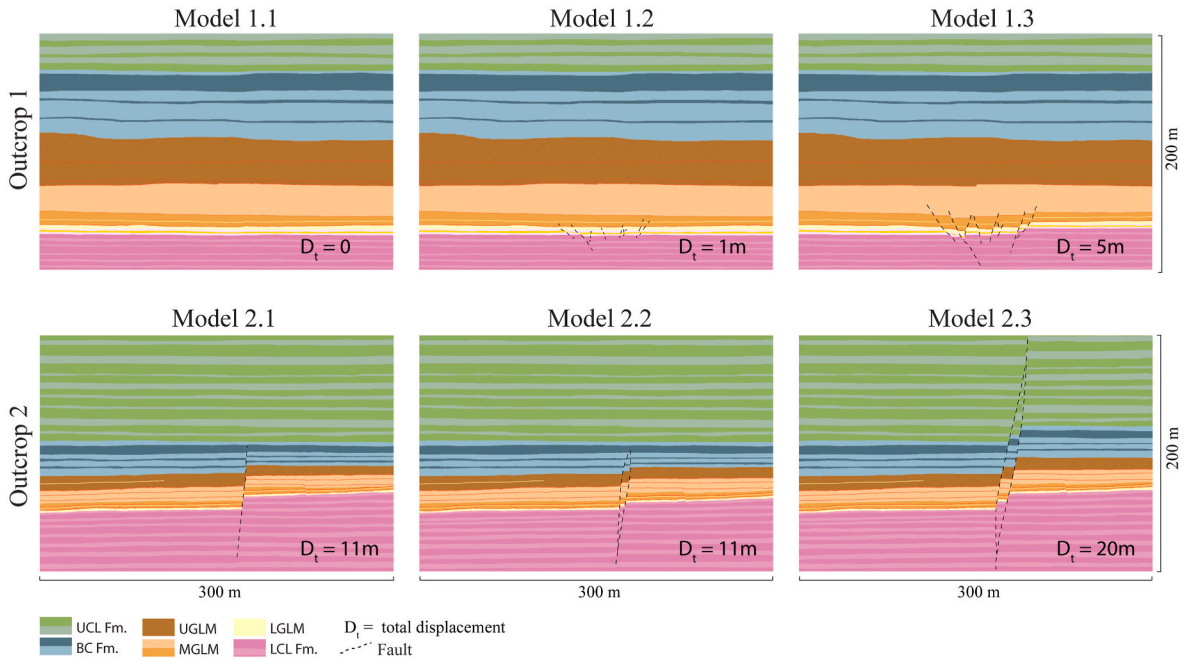


**Fig. 5.** Overview of the six geological 2D models created from the two outcrops at Ras-Ir-Raheb. Model 1.2 and 2.2 gives the most precise portrayal of the actual outcrop 1 and 2, respectfully. All models are 200 × 300 m and scaled 1:1.

geometry was simplified to consist of a single planar fault strand of 11 m offset (Model 2.1), for comparison with a model of the true geometry where the two-strand lens geometry was included (Model 2.2). In Model 2.2, the throw is split between the two fault strands, with a combined displacement of 11 m, i.e., equal to that of the single fault in Model 1.1. The third model (Model 2.3) was created with a total combined displacement across the two-strand fault zone exaggerated to 20 m, where the up-dip (and partly down-dip) extent of the fault was increased.

## 5. Results

We here present the results, starting with the effect the wavelet shape and frequency have on the seismic (Fig. 6), before moving on to the resulting synthetic seismic. With the variables presented in section 4, our models result in 36 different seismic images (Figs. 7 and 8). The results from the two model-series are presented in the following subsections. Model Series 1 are based on Outcrop 1, whereas Model Series 2 are based on Outcrop 2.

### 5.1. Effect of the different seismic wavelet types

The effect of the different wavelet shapes and frequencies can be seen in Fig. 6, where an example of synthetic seismic created with the 30 Hz Ricker (Fig. 6 a) and the Ormsby wavelets (Fig. 6 b) are presented with wiggle trace of both the wavelet and the reflectivity of a chosen line. The wiggle trace clearly shows how the two wavelets affect the seismic images. The wiggle trace for the 30 Hz Ricker wavelet shows little variation in amplitude with few, high-amplitude peaks and troughs (Fig. 6 a), leading to the few and thick reflections we see in the seismic image. The wiggle trace from the Ormsby wavelet is very different, showing several narrower peaks and troughs in the upper half of the wiggle trace before one higher amplitude trough followed by a double peak (Fig. 6 b). The shape of the 30 Hz Ricker wavelet with the negative side lobes leads to a seismic image where only the strongest reflectors show as thick reflections, and anything located too close to these disappear within the side lobes. The negative side lobes contribute to the strong negative reflection we observe in the centre of the image and enhance the adjoining positive reflections. In the seismic image using the Ormsby wavelet (Fig. 6 b), we can see that the negative reflection is weaker than

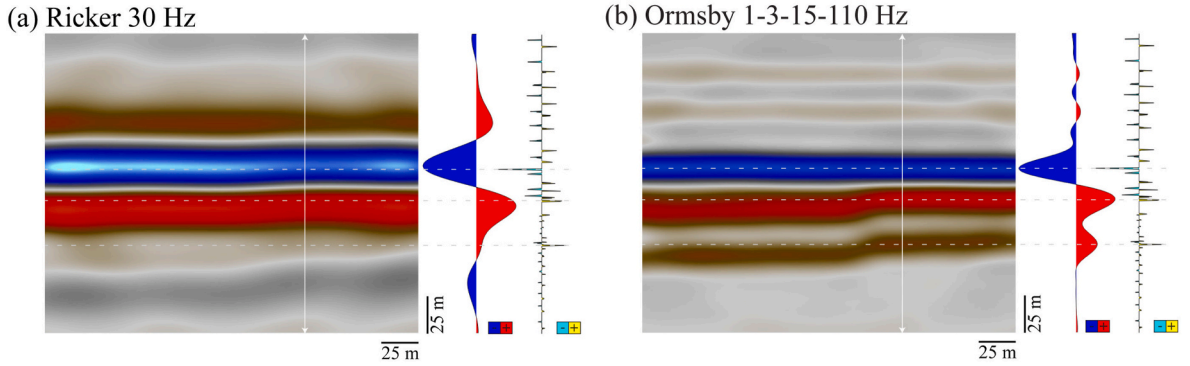


**Fig. 6.** a) Seismic image produced using the 30 Hz Ricker wavelet, with wiggle trace and reflectivity trace on the right – extracted from the placement of the white vertical line in the seismic image. b) Seismic image produced using the Ormsby 1-3-15-110 Hz wavelet, with wiggle trace and reflectivity trace on the right – extracted from the placement of the white vertical line in the seismic image.

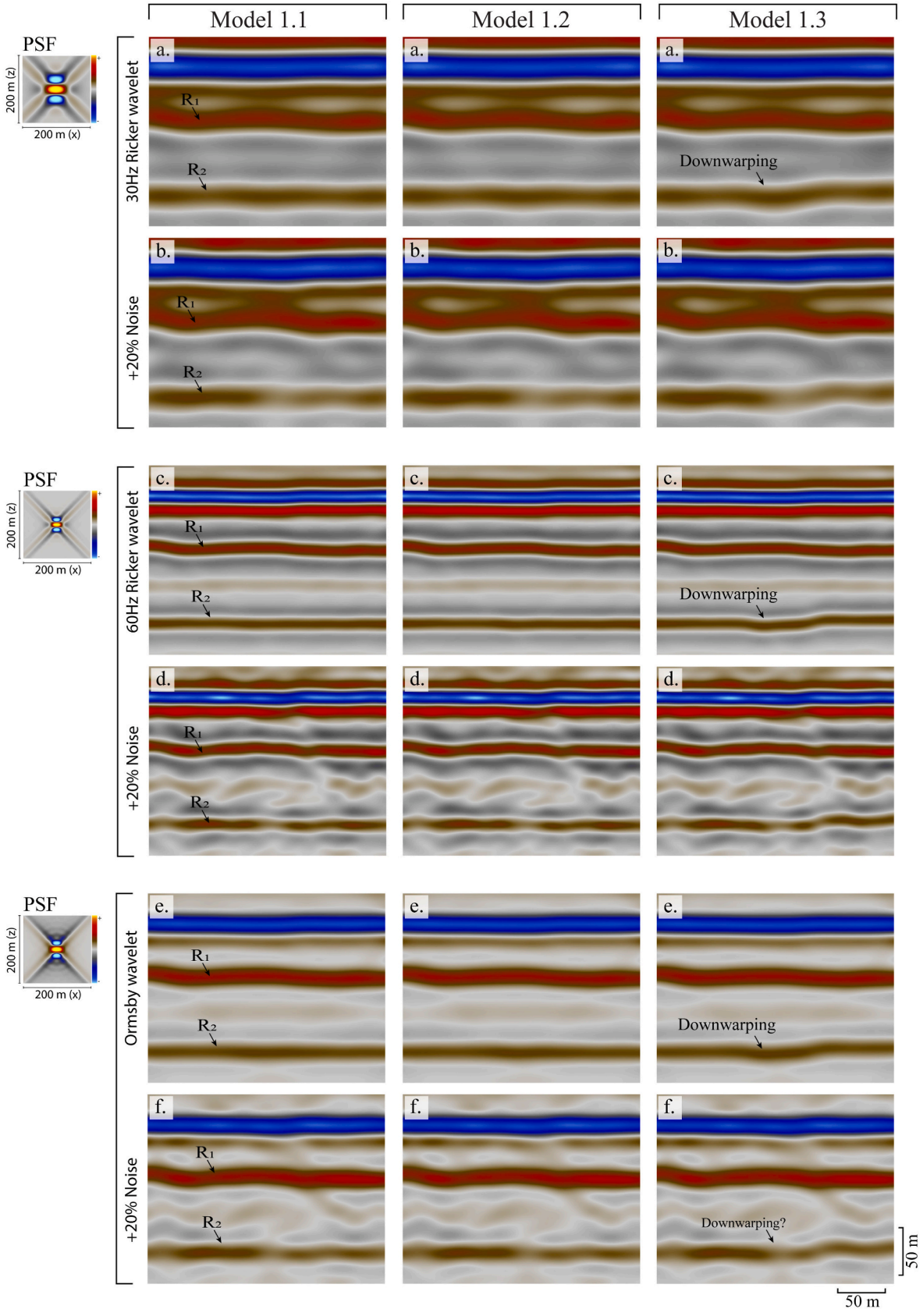


**Fig. 7.** All seismic images within model series 1. Showing the seismic images of Model 1.1 (a–f) vertically on the left, all seismic images of Model 1.2 (a–f) vertically in the middle, and all seismic images of Model 1.3 (a–f) vertically to the right.

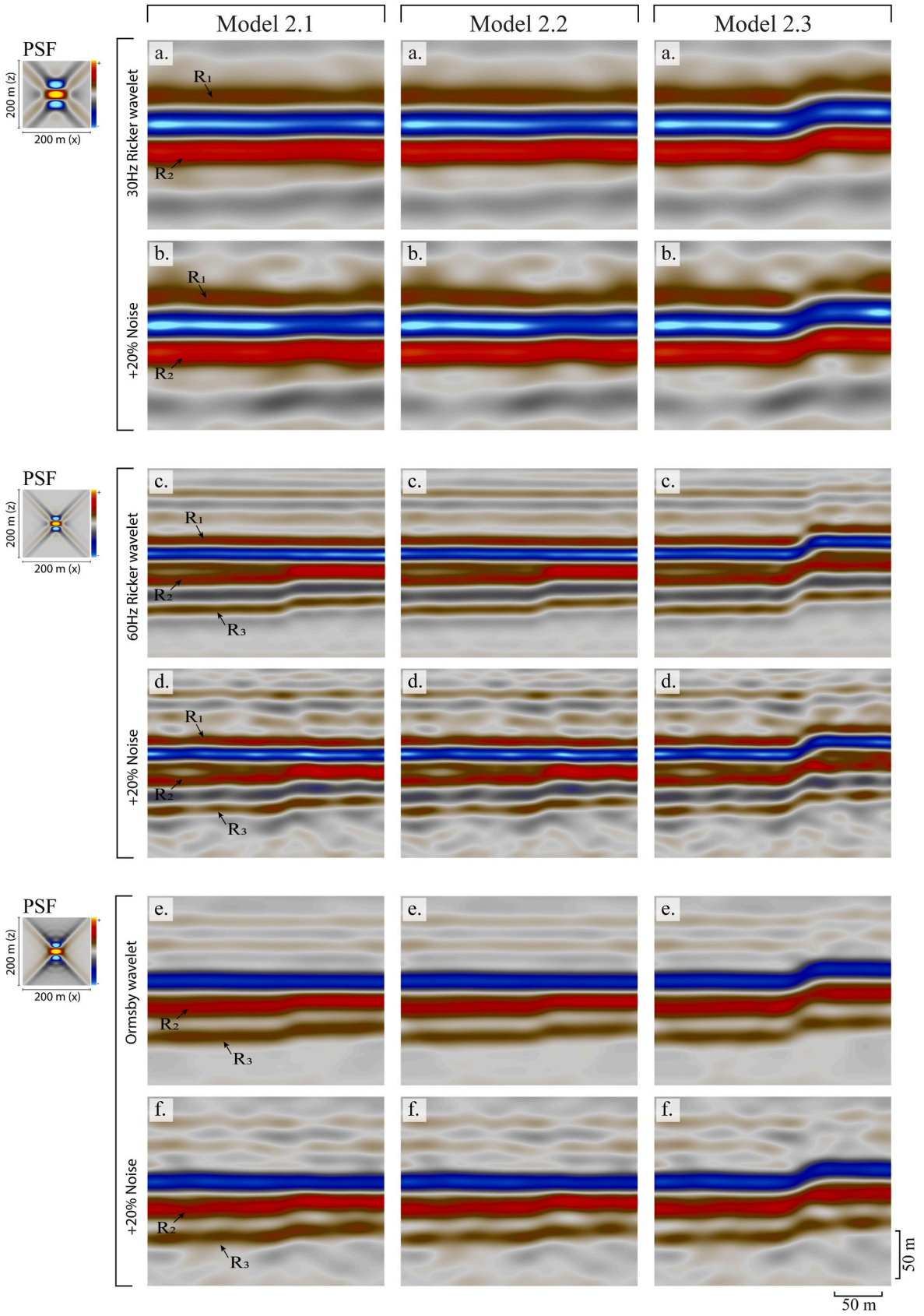


**Fig. 8.** All seismic images within model series 2. Showing the seismic images of Model 2.1 (a–f) vertically on the left, all seismic images of Model 2.2 (a–f) vertically in the middle, and all seismic images of Model 2.3 (a–f) vertically to the right.

in the 30 Hz Ricker image, and the amplitude trough of the wavelet to the right is less wide. Instead of one continuous amplitude peak below the trough of the wavelet we here see two peaks following each other. In the seismic image this is seen as two distinguishable positive reflections. This matches up well with the reflectivity trace on the far right in the figure where we can see corresponding peaks.

### 5.2. Model series 1 (compound graben; 0–5 m displacement)

Common for all the seismic images from Model Series 1 is the strong negative amplitude reflection (blue) seen near the top of all the images, representing the stratigraphic boundary between the Upper Coralline Limestone Fm. and the Blue Clay Fm. (Fig. 7). Additionally, there are two strong positive-amplitude reflections (red) visible throughout all images, called $R_1$ and $R_2$ (marked with arrows in Fig. 7). $R_1$ is the reflection from the boundary between the Upper Coralline Limestone Fm. and the Upper Globigerina Limestone Fm., while $R_2$ is the reflection from the boundary between the Lower Coralline Limestone Fm. and the Lower Globigerina Limestone Fm. The character of these two reflections varies in the different seismic images, due to the changing survey parameters and input geology. The variations of the fault-affected reflection $R_2$ is key to the detailed seismic image descriptions below.

#### 5.2.1. Model series 1 results using the 30 Hz ricker wavelet

The fault-free reference model (Model 1.1, Fig. 7 a), without any structures, produces a very simple seismic image, with Reflection $R_2$ being continuous. The seismic image created with the 30 Hz Ricker wavelet shows strong, sub-horizontal reflections with no reflectivity between $R_1$ and $R_2$. The seismic images of Model 1.2 (Fig. 7 1.2 a) are practically identical to the images of the reference model (Fig. 7 1.1 a), and the small faults have no notable effect on the seismic image. In Model 1.3, the seismic image produced using the 30 Hz Ricker wavelet shows a slight downwarping of reflection $R_2$, in the area of the compound graben with the combined displacement of 5 m (Fig. 7 1.3 a). Adding noise to the seismic images has a limited effect on the images in the 30 Hz Ricker wavelet scenarios (Fig. 7 b).

#### 5.2.2. Model series 1 results using the 60 Hz ricker wavelet

The seismic images based on the 60 Hz Ricker wavelet resolves more reflections, since the vertical seismic resolution is improved relative to the 30 Hz images (Fig. 7 c), and the reflections are narrower and more well-defined. A strong positive reflection (red) can now be observed immediately below the strong negative reflection (blue) that was also seen in the 30 Hz Ricker images, and a lower-amplitude positive reflection can be seen between $R_1$ and $R_2$. Model 1.1 (Fig. 7 1.1 c) and Model 1.2 (Fig. 7 1.2 c) are practically identical, whereas in Model 1.3 (Fig. 7 1.3 c) reflection $R_2$ is downwarped at the location of the compound graben. Compared to the 30 Hz image of Model 1.3, the downwarped part of reflection $R_2$ is slightly more rugose and defined, reflecting more of the detailed structure of the compound graben. Adding noise again distorts the images and results in poorer reflectivity between $R_1$ and $R_2$, and slightly blurs the downwarping of R2 at the location of the compound graben in the seismic image of Model 1.3.

#### 5.2.3. Model series 1 results using the ormsby wavelet

The Ormsby-type wavelet produces seismic images of similar quality to those produced using the 30 Hz Ricker wavelet, but with a 'cleaner' appearance. The reference Model 1.1 (Fig. 7 1.1 e) clearly shows the negative reflection (blue) near the top of the model, as well as the strong, positive reflections $R_1$ and $R_2$. Model 1.2 (Fig. 7 1.2 e) is again identical to the reference model, whereas in Model 1.3 (Fig. 7 1.3 e) we can observe a slight downwarping of reflection $R_1$ as also seen in the images using the Ricker wavelets. The addition of noise to the Ormsby wavelet images still leaves the reflections interpretable, but noise distorts reflectivity between reflections $R_1$ and $R_2$.

### 5.3. Model series 2 (11–20 m displacement)

The negative amplitude marking the stratigraphic boundary between the Upper Coralline Limestone Fm. and the Blue Clay Fm., seen as a strong negative amplitude reflection (blue) in the seismic, is present in all the seismic images produced in the Model 2 series (Fig. 8). Otherwise, the different geological models in combination with the various petrophysical properties created variations within the seismic images that will be described in the following.

#### 5.3.1. Model series 2 results using the 30 Hz ricker wavelet

The single-strand reference Model 2.1 (D = 11 m) shows one negative and two positive strong reflections in the (vertically) central part of the seismic image (Fig. 8 2.1 a). The two positive reflections are marked as $R_1$ and $R_2$. A very weak, positive reflection is shown just below $R_2$, slightly tapering towards the right. The seismic image derived from the double-strand Model 2.2 (combined D = 11 m, Fig. 8 2.2 a) is overall similar to the image of Model 2.1, however, a slight difference can be noticed in the weak reflector below $R_2$, which is here a bit cloudier than in Model 2.1. Importantly, fault offsets are not resolved in neither of the Models 2.1 or 2.2. A more obvious change is seen from the latter two models when looking at Model 2.3 (Fig. 8 2.3 a). The location of the fault is clearly detectable in this seismic image where the fault displacement is exaggerated to 20 m and offsets the boundary between the Upper Globigerina Limestone Member and the Blue Clay Formation (Fig. 8 2.3 a). Although there are no discrete reflection offsets, the offset is imaged as a monoclinal shape of the strong reflections in the vertically middle part of the seismic image. When noise is added to the 30 Hz seismic images (Fig. 8 b), the two strong reflections are still clear but the weak reflection just below $R_2$ are blurrier and partly split. Notably, even when adding noise, the imaging of the fault offsets as a monoclinal geometry remains clear in Model 2.3, whereas in Models 1.1 and 1.2 the reflections remain horizontal.

#### 5.3.2. Model series 2 results using the 60 Hz ricker wavelet

In general, the seismic images produced with the 60 Hz Ricker wavelet exhibit narrower and more well-defined reflectors than the 30 Hz Ricker images (Fig. 8 c and d). In the upper half of the seismic image of the single strand fault model, Model 2.1 (D = 11 m, Fig. 8 2.1 c), we can observe several weaker, horizontal and continuous reflections above $R_1$. $R_1$ is shown as a clear reflection immediately above a strong negative reflection and can be followed continuously from left to right in the image. Reflection $R_2$ can again be found just underneath the negative reflection but appears to be horizontally split in two towards the left side of the image, while stepping up on the right-hand side in a monoclinal shape where it is expressed as one, thicker reflection. Below $R_2$ there is another positive reflection, $R_3$, whit slightly lower amplitude and following the monoclinal shape of $R_2$. The seismic image of the double strand fault model, Model 2.2 (combined D = 11 m, Fig. 8 2.2 c), is almost identical to that of Model 2.1 except for some very slight amplitude strength variations in the stepping part of the monoclinal. More variation is seen when looking at the seismic image of Model 2.3 where the faults displacement is exaggerated to 20 m and breaches all the way through the Upper Coralline Limestone (Fig. 8 2.3 c). Here, all reflections show a monoclinal shape, and Reflection $R_1$ is discretely offset. Reflectivity in the upper and lower part of the model is distorted when noise is added, whereas all reflections in the high-reflective central part of the images are still well-resolved (Fig. 8 d).

#### 5.3.3. Model series 2 results using the ormsby wavelet

The resultant images using the Ormsby wavelet (Fig. 8 e and f) are of a quality and resolution that lies between that of the 30 Hz and the 60 Hz Ricker wavelet images. Considering Model 2.1 (D = 11 m, Fig. 8 2.1 e), the image is dominated by the strong negative reflection (blue) as well as positive reflections $R_2$ and $R_3$. Reflection $R_1$ seen in previous models is no longer observable. Reflections $R_2$ and $R_3$ show a slight monoclinal

shape. The seismic image of Model 2.2 (combined D = 11 m, Fig. 8 2.2 e) is practically identical to that of Model 2.1. The reflectivity pattern of Model 2.3 (combined D = 20 m, Fig. 8 2.3 e) is similar, although in this model all the reflections have a monoclinal shape. Adding noise distorts reflectivity in the upper and lower part of the images and make the uppermost reflections cloudy (Fig. 8 f). The strong negative reflection and $R_2$ appear relatively undisturbed by the noise, while $R_3$ is slightly more rugose (Fig. 8 2.3 f).

## 6. Summary and discussion

Here we summarize and discuss our observations and findings from the seismic, draw comparisons to real seismic data, and comment on the wider implications/applications of our results.

### 6.1. Summary of results

For seismic models without noise, we summarize that:

- compound grabens with cumulative D = 1 m were not visible in the seismic images.
- compound grabens with cumulative D = 5 m were visible in seismic images as a subtle downwarping of reflections.
- single-strand normal faults with D = 11 m were visible as monoclinal distortions of reflections when the quality of the seismic is adequate (60 Hz Ricker wavelet and Ormsby wavelet).
- double strand faults with cumulative D = 20 m were visible in seismic images as discrete reflection offset or as monoclinal reflection geometries.

For seismic models with a seismic-to-noise ratio of 4:1, we summarize that:

- compound grabens with cumulative D < 5 m are reflected only as extremely subtle reflection distortion in the seismic images with noise, and are therefore practically undetectable.
- single-strand normal faults with D = 11 m were visible in the seismic images when the quality of the seismic is adequate (60 Hz Ricker wavelet and Ormsby wavelet).
- double-strand normal faults with cumulative D = 11 m were visible in the seismic images when the quality of the seismic is adequate (60 Hz Ricker wavelet and Ormsby wavelet).
- double-strand normal faults with cumulative D = 20 m were visible as a subtle monoclinal shape of the seismic reflections.

### 6.2. Detectability and effect of small-scale (D = 1–20 m) faults in seismic

Our results indicate that, at signal peak frequencies of 30 Hz (Ricker wavelet) and higher, and *without introducing random noise*, faults down to ~5 m of throw affect the seismic image by slight downwarping of reflections, whereas faults down to ~11 m throw show detectable offsets of reflections in form of a down-stepping monoclinal geometry at signal peak frequencies of 60 Hz (Ricker wavelet). Real seismic will, however, never be noise free even though methods for seismic acquisition and processing have come a long way the last few decades (e.g. Schneider, 1971; Rost and Thomas, 2009; Zhong et al., 2015; Schmelzbach et al., 2016; Li et al., 2018). In our data, the same structures can be identified when noise is included (20% random noise), although the reflections are more irregular and harder to detect. This suggests that under relatively noise-free conditions in high-quality reflection seismic datasets, lower-throw faults (as low as 5 m in this study) that do not induce discrete reflection offsets in seismic images may still produce reflection distortions. As widely documented and discussed in literature (Faulkner et al., 2010), sub-seismic structures such as faults have a large impact on the permeability and fluid flow in the subsurface (e.g. Shipton et al., 2002), and these results are examples that may help seismic interpreters infer what observed distortions in real seismic data may reflect geologically, and highlights how seismic modelling adds further value and insight to the use of outcrop analogues to understand subsurface geology as imaged by seismic.

### 6.3. Wavelet and resolution effects

#### 6.3.1. Seismic wavelets and their effect on the seismic image

The shape of the wavelet is a fundamental aspect of seismic interpretation (Simm and Bacon, 2014), and is also crucial for the results herein. The Ricker wavelet is commonly used in seismic modelling (Eide et al., 2017; Rabbel et al., 2018; Wrona et al., 2020) due to its simple structure, while studies using the more realistic Ormsby wavelet in seismic modelling is until now lacking. We will therefore discuss the differences of the two wavelet types here.

Generally, the 60 Hz Ricker wavelet has a narrower peak in time, due to a wider frequency bandwidth, compared to the Ormsby and 30 Hz Ricker wavelets, thus giving higher-quality seismic images with a higher number of distinguishable reflections, showing more detail. The Ormsby wavelet and Ricker wavelets have very similar peaks in time but where the Ormsby wavelet have several small side lobes with almost no negative parts, the Ricker wavelets have only two, but much more pronounced negative side lobes (Fig. 3).

So, although the peaks of the 30 Hz Ricker wavelet and the Ormsby wavelet are very similar (as presented in Fig. 3), their seismic expression becomes very different due to the side lobes, as showed in Fig. 6. While the "lack" of side lobes in the Ormsby wavelet provide higher vertical resolution and produce a cleaner seismic image, the side lobes of the 30 Hz Ricker wavelet interfere with the reflectors in the model and disturb the signal. In many ways, the seismic response of the Ormsby wavelet is more like that of the 60 Hz Ricker wavelet. It is important to note that the effects from the side lobes affect the seismic in all directions; herein we look at 2D images but in 3D we would have to consider such effects in a three-dimensional manner and nearby lateral reflectivity may affect the trace. Additionally, all reflectivity might not be illuminated, depending on the dip of the underlying strata.

From our data, we can observe that the shape of the Ormsby wavelet gives a better result. The Ricker wavelet has been criticized in literature earlier, and already in 1988, Hosken (1988) published his scepticism towards the extended use of the Ricker wavelet (especially in the industry), and simply concluded that "*Ricker wavelets should never be used*". However the simplicity of the Ricker wavelet makes it very convenient for the creation of synthetic data, and it is still commonly used (e.g. Eide et al., 2017; Wrona et al., 2020). Contrary to other wavelet types (e.g. Ormsby, Butterworth) the Ricker wavelet can be described by its peak frequency and a relatively simple mathematical equation (Ryan, 1994). "Real" seismic wavelets from surveys, however, are more complex and usually asymmetrical in respect to time, opposed to the symmetrical Ricker wavelet (Wang, 2015). Hence, our asymmetrical Ormsby wavelet, which mimics a real seismic wavelet, is a better option for creating synthetic seismic that is more like real seismic.

However, the wavelets shape and behaviour may vary, and Andersen (2020) concludes in her MSc thesis that a 40 Hz Ricker wavelet is more suitable than a 5-10-60-90 Hz Ormsby wavelet for seismic modelling. To get a better understanding of the difference between the three seismic wavelets we used herein, we have superimposed their wiggle traces altogether in Fig. 9 and placed them alongside the corresponding reflectivity trace.

Looking at the 30 Hz Ricker wavelet vs. the Ormsby wavelet we can see the effect the different wavelet shapes have on the wiggle trace and hence the seismic images; a high-amplitude trough at the top followed by a peak that for the Ormsby wavelet can be observed as two peaks, but for the 30 Hz Ricker wavelet is more continuous. Below these, at 100–150 m depth, we can see a trough of the 30 Hz Ricker wavelet with two trough-maximums at about 110 m and 140 m depth, whereas the Ormsby wavelet show no negative part here but a small peak in the

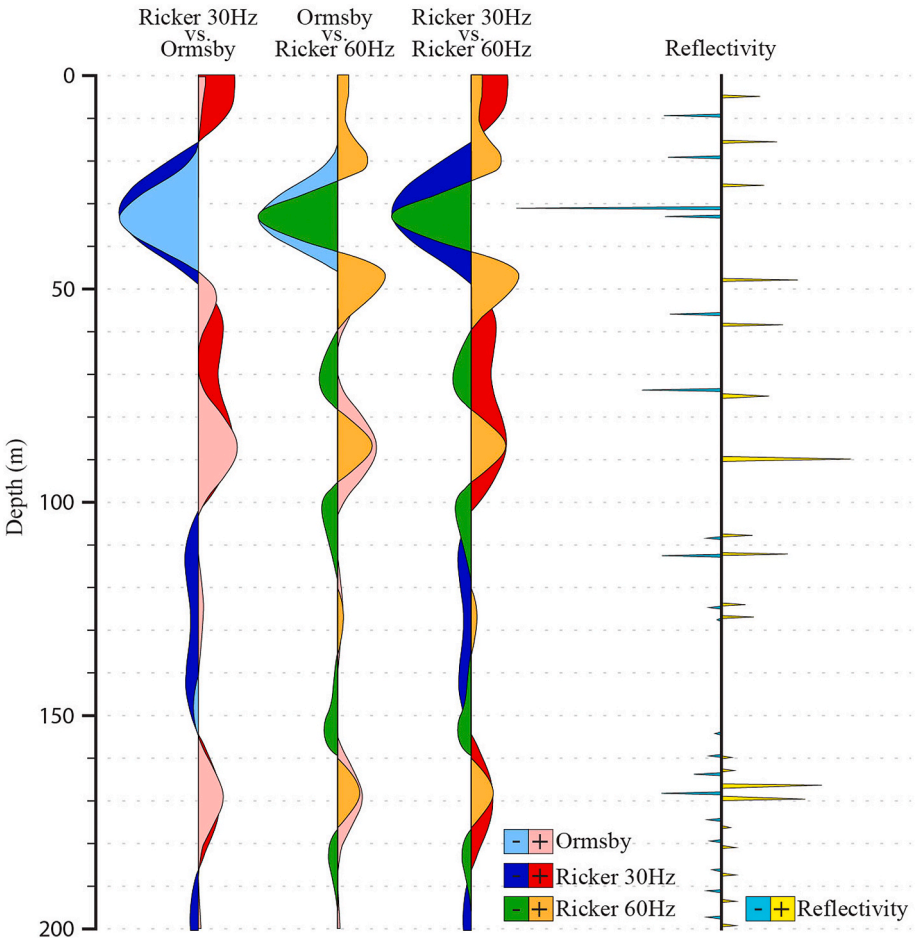


**Fig. 9.** Wiggle trace of the three wavelets used herein, superimposed to allow for comparison. The associated reflectivity trace to the right in the figure allows for comparison between reflectivity and seismic wave pattern.

middle, at about 125 m depth. Looking at the Ormsby wavelet vs. the 60 Hz Ricker wavelet, we see more similarities on the positive side of the wiggle trace where all peaks are found at the same places. On the negative side however, we can still only observe the one trough at the uppermost part of the wiggle trace for the Ormsby wavelet, while the 60 Hz Ricker wiggle trace show several troughs throughout, alternating with the peaks. The two Ricker wavelets are similar in the way that they both have alternating peaks and troughs along the wiggle trace. However, due to the narrower amplitude spectra and wider bandwidth of the 60 Hz Ricker wavelet, the 60 Hz Ricker wiggle trace better distinguish and show the various events (peaks and troughs). When comparing the wiggle traces to the reflectivity trace, it is evident that (especially from 170 m and below) the closely spaced events with opposite polarity eradicate each other and hence do not show in any of the wiggle traces.

### 6.3.2. *Resolution effects*

Related to the wavelet shapes and their corresponding frequency bandwidth is the vertical and horizontal seismic resolution. The seismic resolution controls the ability of seismic reflection data to image geological features, including faults and fault zones (e.g. Osagiede et al., 2014; Alaei and Torabi, 2017). We often tend to focus on the vertical resolution, i.e., the minimum vertical distance between two features (reflectors) that are possible to define separately rather than as one (e.g. Chopra et al., 2006; Osagiede et al., 2014), but as we will discuss here, the horizontal resolution is equally important (cf. Faleide et al., 2021). To elucidate this, we will consider the seismic image of Model 2.3 with the 60 Hz Ricker wavelet as an example (Fig. 10). Here, the positive reflection $R_1$ shows a discrete offset in the area where the fault is cutting through. Further down in the seismic image, reflection $R_3$ shows a monoclinal shape and is stepping up where the fault cuts through. This is similar to what we can often see with e.g. sill intrusions and related bridges in sedimentary basins; the bridges are often resolved only as kinks on the sill reflections rather than as discrete reflection discontinuities, and knowledge of sill geometries from nature is necessary for a sound geological interpretation (see e.g. Magee et al., 2015; Eide et al., 2017).

In the geological model and hence also the reflectivity model (Fig. 10 a), the total displacement of the reflector for reflection $R_3$ is slightly larger than that of the reflector for reflection $R_1$. Therefore, one would perhaps initially assume that in a seismic image, the offset would be more easily detected in reflection $R_3$ than in $R_1$, if we consider vertical resolution only. However, the fault lens is also slightly wider at the point where it cuts through $R_3$, and hence the horizontal distance between the two faults bounding the lens is slightly wider for $R_3$ than for $R_1$. As a consequence, despite the reflector for $R_3$ having a larger total offset, reflection $R_3$ shows as a monoclinal shape rather than being resolved as discrete reflection offsets in the seismic image due to a combination of two resolution effects: firstly, the offsets of the two faults are resolved individually, as they are sufficiently far apart to be seen as separate features (the fault distance being greater than *horizontal* seismic resolution); secondly, however, with total fault offset effectively being split across two faults when the two are resolved individually rather than as one, each individual fault offset then falls below the *vertical* seismic resolution. The reflectivity model (Fig. 10 a) has been superimposed with the synthetic seismic (Fig. 10 b) in Fig. 10 c to illustrate this resolution effect. Similar effects may be seen e.g., with narrow and closely

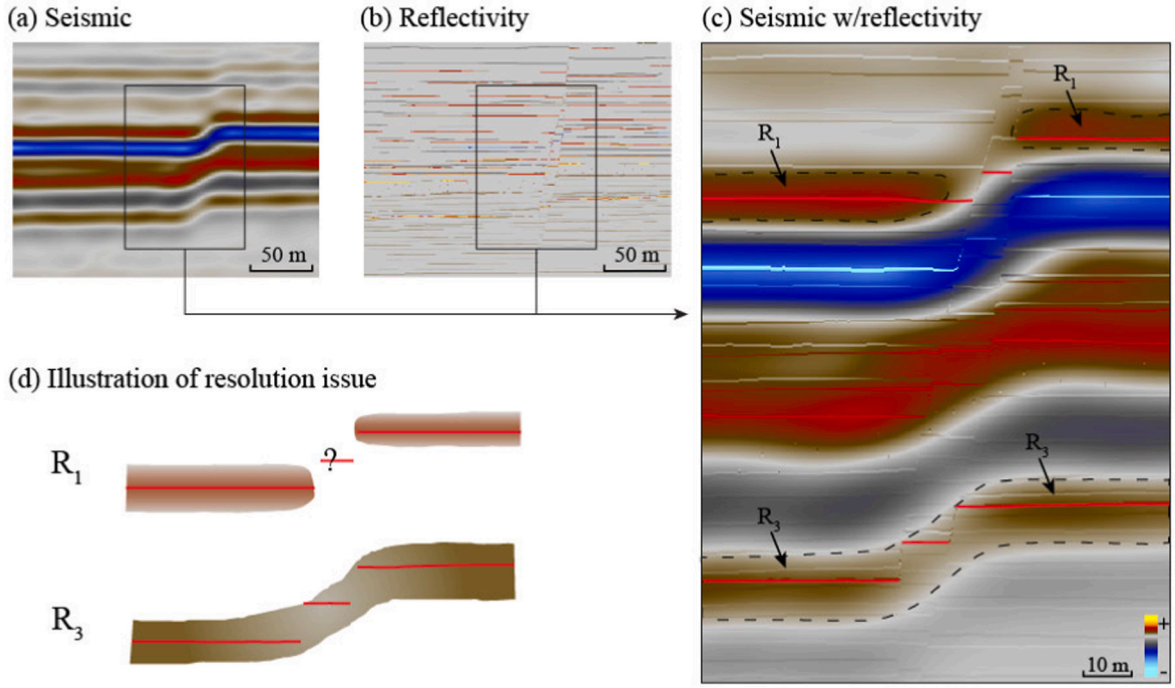


**Fig. 10.** a) seismic image of Model 2.3 using the Ricker 60 Hz wavelet are superimposed with the reflectivity model. The reflectors of $R_1$ and $R_3$ are highlighted by bright red color for easier identification across the image. b) Illustration of the difference of the imaging of reflector $R_1$ and $R_3$. (For interpretation of the references to colour in this figure legend, the reader is referred to the Web version of this article.)

spaced fluvial channels or channel belts in seismic images, that are difficult to separate as individual depositional objects (e.g. Al-Masgari et al., 2021). The fault offsets are therefore resolved as a monoclinal geometry rather than as discrete reflection offsets for reflection $R_3$. For reflection $R_1$ on the other hand, the (shorter) distance between the two faults bounding the fault lens falls below *horizontal* seismic resolution. This has the effect that the two faults cannot be resolved individually and are 'seen' as one fault, and with the throws of the two faults combined, the total offset is greater than the *vertical* seismic resolution, and the fault offset of Reflection $R_1$ is therefore resolved discretely (Fig. 10 d).

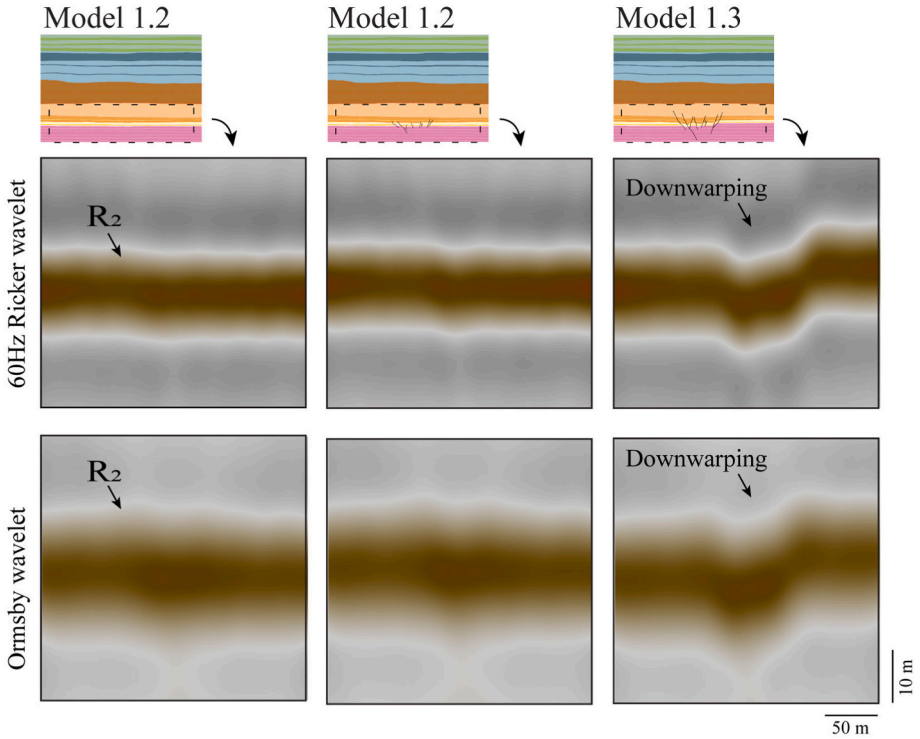


**Fig. 11.** Areas of interest in the seismic images of Model series 1, with a vertical exaggeration with the factor of five. Noise is not included.

### 6.4. Relevance to practical seismic interpretation and comparisons with real seismic data

#### 6.4.1. Vertical exaggeration in seismic interpretation

When interpreting seismic data, interpreters often use vertical exaggeration to better visualize and interpret the imaged geologic features in the vertical dimension, such as faults, dykes, stratigraphic boundaries, unconformities etc. (Stewart, 2011; Alcalde et al., 2019). To make our results more applicable, we will therefore look at some of the more interesting areas of our synthetic seismic where the Y-axis (depth) is exaggerated by a factor of 5 (Figs. 11 and 12). Noise was not included in these images as our previous results showed that the main features were still visible with a seismic-to-noise ratio of 4:1, and we want instead to check if any distortion caused by the smaller faults (with D $\leq$ 1 m) would be easier to pick up with vertical exaggeration. Exaggerating the vertical scale of the seismic images of model series 1 (Fig. 11) does not bring any change to our initial summary of observations. We here present the results using the 60 Hz Ricker and the Ormsby wavelets; no observable change can be seen in the seismic images of Model 1.1 vs. 1.2, hence we can conclude faults with displacement $\leq$1 m are not detectable in seismic, even with vertical exaggeration. The downwarp of $R_2$ in the seismic images of Model 1.3 is still visible but may actually be harder to observe in the seismic images with the Ormsby wavelet as vertically exaggerated reflection irregularities obtuse the feature. With the 60 Hz Ricker wavelet, however, the downwarp of the reflection becomes more prominent in the seismic image and hence makes the graben easier to detect.

When studying the seismic images of the Model 2 series in Fig. 7, no visible difference between the seismic images of the single strand fault (Model 2.1) and the double strand fault (Model 2.2) were observed. To see if any changes could be detected, the seismic images with the highest seismic resolution (60 Hz Ricker wavelet) were vertically exaggerated by a factor of 5 (Fig. 12). Considering Fig. 12, only a very slight increase in amplitude can be seen just at the bend of the monocline in the vertically exaggerated seismic image of Model 2.1 (marked by a red arrow in Fig. 12) compared to the seismic image of Model 2.2. When applying vertical exaggeration to the seismic image of Model 2.3 (Fig. 12) the offset of reflection $R_1$ and the monoclinal shape of reflections $R_2$ and $R_3$ are easier to observe.

In summary, increased vertical exaggeration may help the identification of subtle reflection distortions or offsets (Stewart, 2011, 2012); however, their geological interpretation will be uncertain and may rely more on the interpreter's conceptual understanding of subseismic faulting as well as of local geology. This may involve a more conceptual approach to seismic interpretation, which is associated with certain pitfalls. For example, the study by Alcalde et al. (2019) show that early anchoring into specific conceptual models may introduce bias to the interpretation of faults from seismic reflection data. However, the same study showed that increasing vertical exaggeration had limited effects of introducing bias in fault interpretations. Such a conceptual bias may not be negative but may actually be a desired conceptual bias that for example favours the interpretation of faults in an area where faults are to be expected. As such, provided that such conceptual bias is used purposely, we suggest it may help achieve a geologically overall sounder interpretation.

#### 6.4.2. Comparison with real seismic data

We here compare our results with an image from a high-quality, high-resolution 3D reflection seismic dataset from the SW Barents Sea, as previously mentioned. Comparing our results with real seismic data provides an opportunity to put our synthetic seismic in context of a real seismic dataset with similar lithology/geology. Our Ormsby-wavelet was created to match that of the interval of interest in the real seismic data, a carbonate-dominated succession near the crest of a rotated fault block. Furthermore, the rock properties within our models are comparable to those expected at the burial depths of the interval of interest in the real seismic data as described earlier. Comparing our models with the real seismic, several subtle features in the actual seismic reflection images show similarities to our synthetic seismic images. Fig. 13 shows a seismic image from the real data set and side-by-side comparisons with examples from the synthetic images for comparison.

In Fig. 13 a, small bend in the reflections (marked by the arrow) can

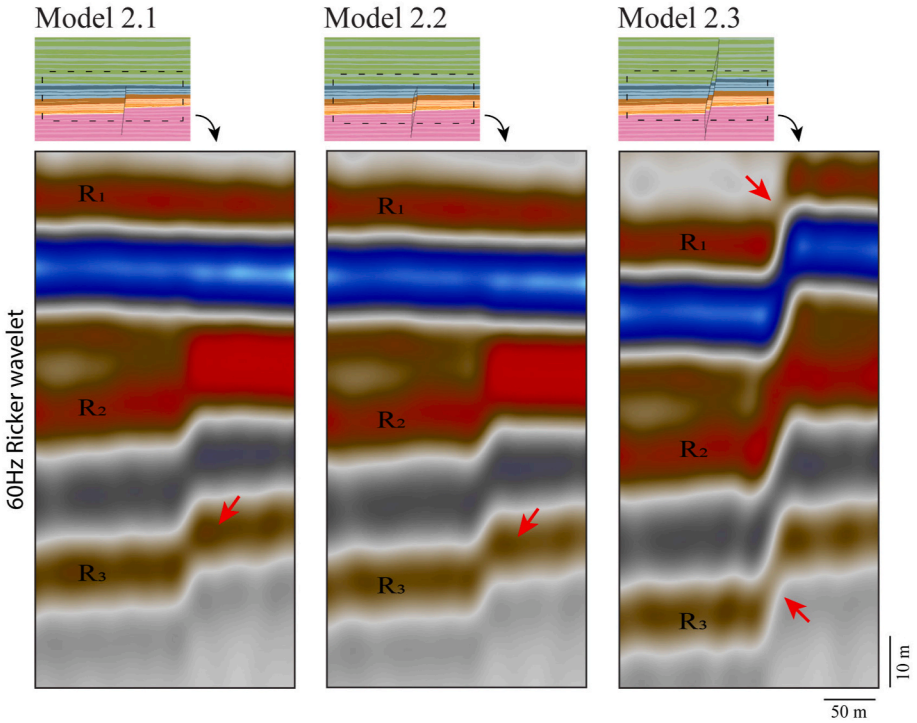


**Fig. 12.** Areas of interest in the seismic images of Model series 2, with the 60 Hz Ricker wavelet and a vertical exaggeration with the factor of five. Noise is not included.

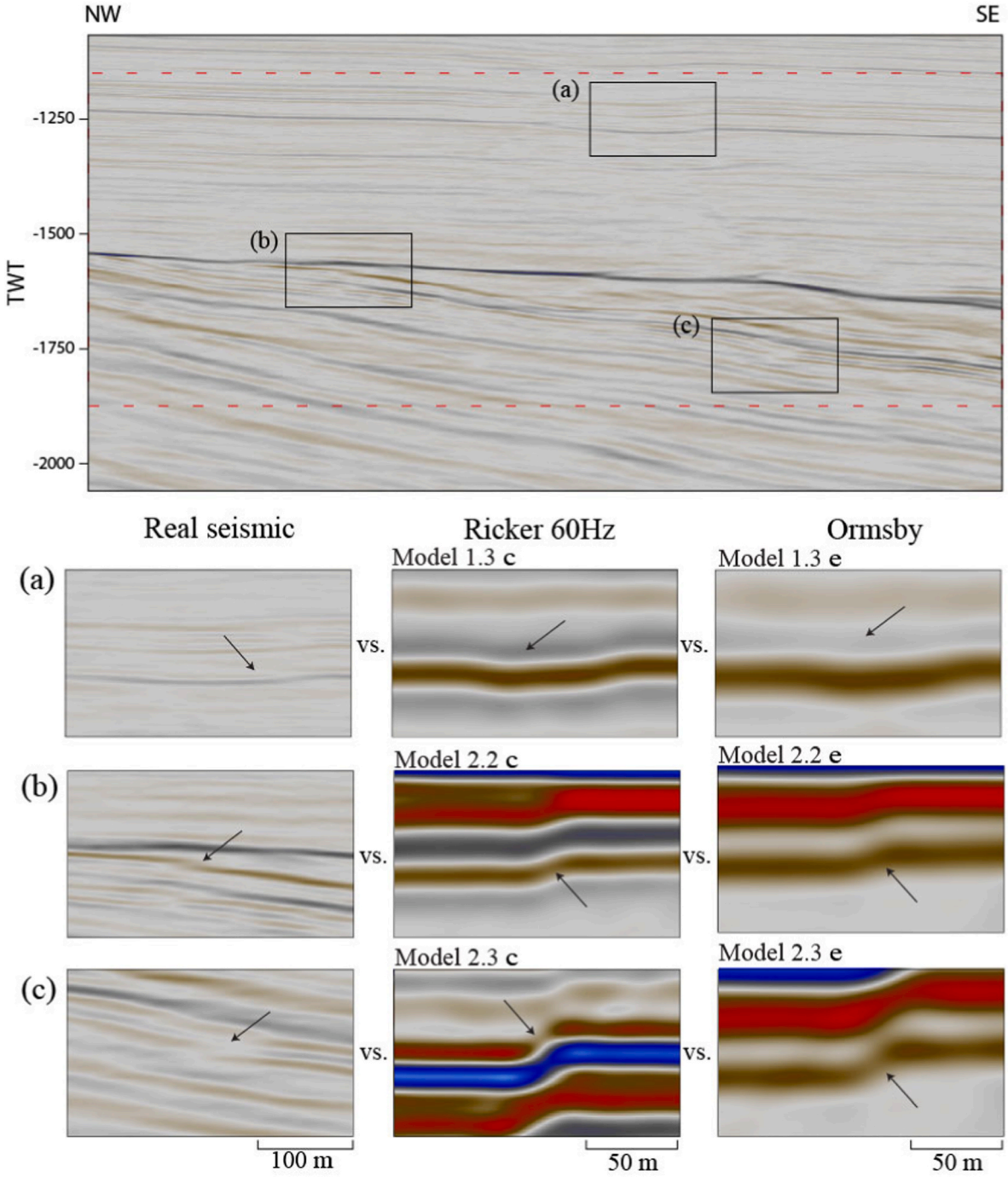


**Fig. 13.** Example of real seismic data (Topseis) from the SW Barents Sea for comparison with our results. a) Example of a slight downwarping geometry b) example of monoclinal shaped reflection c) example with descrete offset of reflections.

be seen in the overburden above the rotated fault block, giving the reflections a graben like, downwarping geometry - similar in appearance to that observed in the synthetic seismic images of Model 1.3. The seismic sections shown in Fig. 13 b and c are found deeper in the stratigraphy (at reservoir level), near the crest of the rotated fault block. In Fig. 13 b we can see an example of a monoclinal geometry in the real seismic data, similar to that observed in the seismic images of Model 2.2, both when using the 60 Hz Ricker wavelet and the Ormsby wavelet. The example in Fig. 13 c show a discrete offset of a positive amplitude reflection in the real seismic, similar to what we can observe in reflection $R_1$ above the strong negative amplitude reflection in the seismic image of Model 2.3 with the 60 Hz Ricker wavelet. From using the Ormsby wavelet, a similar but not as clear example to compare with can be found in reflection $R_2$, just below the strong negative reflection.

The results from this study do not constitute evidence that the reflection distortions seen in the real seismic are caused by discrete faults. However, our seismic modelling results do demonstrate that faults with throws at or below seismic resolution may indeed cause such subtle reflection distortions, which are common features in seismic images of faulted strata. Our results therefore provide an empirical basis for geological interpretation of such subtle reflection distortions.

## 7. Concluding remarks

We have addressed the question of how small-scale faults (D = 1–20 m) affect seismic images, and whether such faults may be observed or inferred from the seismic images, for several given seismic survey conditions and parameters. We found that within relatively noise-free, high-quality reflection seismic datasets, faults with offsets down to 5 m may cause distortions and downwarping geometries to reflections that may help seismic interpreters infer or hypothesize their presence. Somewhat larger normal faults and normal fault pairs (here, D = 11–20 m) may cause discrete reflection offsets, or monoclinal shape of reflections, depending on the horizontal and lateral seismic resolution of the dataset. It is worth noting that although small scale faults down to a few meters of throw may distort reflections, the inference of faults from subtle reflection distortions in real seismic data is inherently uncertain. Nevertheless, evidence from studies such as this may offer empirical support for more geologically concept-driven interpretation strategies, for example suggesting that in certain geological settings, subtle reflection distortions should generally be interpreted as discrete faults. Although previous studies have pointed out the biases and potential pitfalls of conceptually driven fault interpretation (Alcalde et al., 2019), we suggest that when used with caution a concept driven approach may be justified.

## Declaration of competing interest

The authors declare that they have no known competing financial interests or personal relationships that could have appeared to influence the work reported in this paper.

## Data availability

Data will be made available on request.

## Acknowledgements

We acknowledge funding for a personal PhD grant for Vilde Dimmen from VISTA – a basic research program in collaboration between The Norwegian Academy of Science and Letters, and Equinor (grant number 6272). We further acknowledge NORSAR for an academic license of the seismic modelling software SeisRoX. The virtual outcrop was partly visualized and interpreted using LIME (http://virtualoutcrop.com/lime). We are grateful to Lundin Energy Norway for access and permission to publish the seismic image shown in Fig. 13, and to Roy Davies, Jostein Herredsvela and Wintershall DEA for helpful discussions. Dr. David Peacock is thanked for invaluable assistance during data collection in Malta. We are grateful to the reviewers Dr. Charlotte Botter and Dr. Alexandre Maul for their constructive reviews that helped improve the final version of this manuscript. We also acknowledge Dr. Marcos Fetter and Dr. Massimo Zecchin for helpful and constructive editorial handling.

## References

Al-Masgari, A.A.-S., Elsaadany, M., Siddiqui, N.A., Latiff, A.H.A., Bakar, A.A., Elkurdy, S., Hermana, M., Babikir, I., Imran, Q.S., Adeleke, T., 2021. Geomorphological geometries and high-resolution seismic sequence stratigraphy of Malay basin's fluvial succession. Appl. Sci. 11, 5156. https://doi.org/10.3390/app11115156.

Alaei, B., Torabi, A., 2017. Seismic imaging of fault damaged zone and its scaling relation with displacement. Interpretation 5, SP83–SP93. https://doi.org/10.1190/INT-2016-0230.1.

Alcalde, J., Bond, C.E., Johnson, G., Kloppenburg, A., Ferrer, O., Bell, R., Ayarza, P., 2019. Fault interpretation in a vertically exaggerated seismic section: evidence of conceptual model uncertainty and anchoring. Solid Earth Discussions 1–20. https://doi.org/10.5194/se-2019-66.

Andersen, I.G., 2020. Effects of Geophysical Parameters on the Seismic Expression of the Maghlaq Fault, Malta: Insights from Outcrop-Based 2D Seismic Modeling, Mathematic and Natural Sciences. University of Bergen, p. 102.

Anselmetti, J.D., Eberli, G.P., 1993. Controls on sonic velocities in carbonates. Pure and Applied Geophysics 141, 287–323. https://doi.org/10.1007/BF00998333.

Aydin, A., 2000. Fractures, faults, and hydrocarbon entrapment, migration and flow. Mar. Petrol. Geol. 17, 797–814. https://doi.org/10.1016/S0264-8172(00)00020-9.

Bense, V.F., Person, M.A., 2006. Faults as conduit-barrier systems to fluid flow in siliciclastic sedimentary aquifers. Water Resour. Res. 42 https://doi.org/10.1029/2005WR004480.

Beukes, N.J., Gutzmer, J., Mukhopadhyay, J., 2013. The geology and genesis of high-grade hematite iron ore deposits. B. Appl. Earth Sci. 112, 18–25. https://doi.org/10.1179/037174503225011243.

Bonson, C.G., Childs, C., Walsh, J.J., Schopfer, M.P.J., Carboni, V., 2007. Geometric and kinematic controls on the internal structure of a large normal fault in massive limestones: the Maghlaq Fault, Malta. J. Struct. Geol. 29, 336–354. https://doi.org/10.1016/j.jsg.2006.06.016.

Botter, C., Cardozo, N., Hardy, S., Lecomte, I., Paton, G., Escalona, A., 2016. Seismic characterisation of fault damage in 3D using mechanical and seismic modelling. Mar. Petrol. Geol. 77, 973–990. https://doi.org/10.1016/j.marpetgeo.2016.08.002.

Bradaric, A.D., Andersen, T., Lecomte, I., Løseth, H., Eide, C.H., 2022. Recognition and characterization of small-scale sand injectites in seismic data: implications for reservoir development. J. Geol. Soc. 179 https://doi.org/10.1144/jgs2021-041.

Buckley, S.J., Ringdal, K., Naumann, N., Dolva, B., Kurz, T.H., Howell, J.A., Dewez, T.J., 2019. LIME: software for 3-D visualization, interpretation, and communication of virtual geoscience models. Geosphere 15, 222–235. https://doi.org/10.1130/GES02002.1.

Caine, J.S., Forster, C.B., 1999. Fault zone architecture and fluid flow: insights from field data and numerical modeling. Faults and Subsurface Fluid Flow in the Shallow Crust 101–127.

Castagna, J.P., Batzle, M.L., Kan, T.K., Backus, M.M., 1993. Rock Physics - The Link Between Rock Properties and AVO Response: *Offset-Dependent Reflectivity—Theory and Practice of AVO Analysis*. Investigations in Geophysics, Soc. Expl. Geophys., Tulsa, Oklahoma. 8, 135–171.

Cavazza, W., Wezel, F.C., 2003. The Mediterranean region - a geological primer. Episodes 26, 160–168. https://doi.org/10.18814/epiiugs/2003/v26i3/002.

Chen, T., Huang, L., 2015. Directly imaging steeply-dipping fault zones in geothermal fields with multicomponent seismic data. Geothermics 57, 238–245. https://doi.org/10.1016/j.geothermics.2015.07.003.

Chopra, S., Castagna, J., Portniaguine, O., 2006. Seismic resolution and thin-bed reflectivity inversion. CSEG recorder 31, 19–25. https://doi.org/10.1190/1.2369941.

Damsleth, E., Sangolt, V., Aamodt, G., 1998. Sub-seismic faults can seriously affect fluid flow in the njord field off western Norway-a stochastic fault modeling case study. In: SPE Annual Technical Conference and Exhibition. Society of Petroleum Engineers.

Dart, C.J., Bosence, D.W.J., Mcclay, K.R., 1993. Stratigraphy and structure of the Maltese graben system. J. Geol. Soc. 150, 1153–1166. https://doi.org/10.1144/gsjgs.150.6.11.

Dey, A.K., Stewart, R.R., 1997. Predicting density using vs and Gardner's relationship. CREWES Res Rep 9, 1–9.

Dimmen, V., 2016. Structural Controls on Fluid Flow in Carbonate Rocks: Quantitative Insights from the Maltese Islands. MSc. thesis. Department of Earth Science. University of Bergen, p. 88.

Dimmen, V., Rotevatn, A., Nixon, C.W., 2020. The relationship between fluid flow, structures, and depositional architecture in sedimentary rocks: an example-based overview. Geofluids 2020, 211–230. https://doi.org/10.1155/2020/3506743, 2020.

Dimmen, V., Rotevatn, A., Peacock, D.C., Nixon, C.W., Nærland, K., 2017. Quantifying structural controls on fluid flow: insights from carbonate-hosted fault damage zones on the Maltese Islands. J. Struct. Geol. 101, 43–57. https://doi.org/10.1016/j.jsg.2017.05.012.

Eide, C.H., Schofield, N., Lecomte, I., Buckley, S.J., Howell, J.A., 2017. Seismic interpretation of sill complexes in sedimentary basins: implications for the sub-sill imaging problem. J. Geol. Soc. 175, 193–209. https://doi.org/10.1144/jgs2017-096.

Faleide, T.S., Braathen, A., Lecomte, I., Mulrooney, M.J., Midtkandal, I., Bugge, A.J., Planke, S., 2021. Impacts of seismic resolution on fault interpretation: insights from seismic modelling. Tectonophysics 816. https://doi.org/10.1016/j.tecto.2021.229008.

Faulkner, D.R., Jackson, C.A.L., Lunn, R.J., Schlische, R.W., Shipton, Z.K., Wibberley, C.A.J., Withjack, M.O., 2010. A review of recent developments concerning the structure, mechanics and fluid flow properties of fault zones. J. Struct. Geol. 32, 1557–1575. https://doi.org/10.1016/j.jsg.2010.06.009.

Gardner, G., Gardner, L., Gregory, A., 1974. Formation velocity and density—the diagnostic basics for stratigraphic traps. Geophysics 39, 770–780. https://doi.org/10.1190/1.1440465.

Gartrell, A., Zhang, Y.H., Lisk, M., Dewhurst, D., 2004. Fault intersections as critical hydrocarbon leakage zones: integrated field study and numerical modelling of an example from the Timor Sea, Australia. Mar. Petrol. Geol. 21, 1165–1179. https://doi.org/10.1016/j.marpetgeo.2004.08.001.

Grippa, A., Hurst, A., Palladino, G., Lacopini, D., Lecomte, I., Huuse, M., 2019. Seismic imaging of complex geometry: forward modeling of sandstone intrusions. Earth Planet Sci. Lett. 513, 51–63. https://doi.org/10.1016/j.epsl.2019.02.011.

Gueguen, E., Doglioni, C., Fernandez, M., 1998. On the post-25 Ma geodynamic evolution of the western Mediterranean. Tectonophysics 298, 259–269. https://doi.org/10.1016/S0040-1951(98)00189-9.

Haines, T.J., Michie, E.A.H., Neilson, J.E., Healy, D., 2016. Permeability evolution across carbonate hosted normal fault zones. Mar. Petrol. Geol. 72, 62–82. https://doi.org/10.1016/j.marpetgeo.2016.01.008.

Hatton, C., Main, I., Meredith, P., 1994. Non-universal scaling of fracture length and opening displacement. Nature 367, 160–162. https://doi.org/10.1038/367160a0.
Healy, D., Neilson, J.E., Haines, T.J., Michie, E.A., Timms, N.E, Wilson, M.E., 2015. An Investigation of Porosity–velocity Relationships in Faulted Carbonates Using Outcrop Analogues. Geological Society, London, Special Publications 406, 261–280. https://doi.org/10.1144/SP406.13.
Hosken, J., 1988. Ricker wavelets in their various guises. First Break 6 (1), 24–33. https://doi.org/10.3997/1365-2397.1988002.
Jafarian, E., de Jong, K., Kleipool, L.M., Scheibner, C., Blomeier, D.P., Reijmer, J.J., 2018. Synthetic seismic model of a Permian biosiliceous carbonate–carbonate depositional system (Spitsbergen, Svalbard Archipelago). Mar. Petrol. Geol. 92, 78–93. https://doi.org/10.1016/j.marpetgeo.2018.01.034.
Jongsma, D., van Hinte, J.E., Woodside, J.M., 1985. Geologic structure and neotectonics of the North African continental margin south of Sicily. Mar. Petrol. Geol. 2, 156–179. https://doi.org/10.1016/0264-8172(85)90005-4.
Knapp, R.W., 1990. Vertical resolution of thick beds, thin beds, and thin-bed cyclothems. Geophysics 55 (9), 1183–1190. https://doi.org/10.1190/1.1442934.
Krawczyk, C.M., Tanner, D.C., Henk, A., Trappe, H., Ziesch, J., Beilecke, T., Aruffo, C.M., Weber, B., Lippmann, A., Görke, U.J., 2015. Seismic and sub-seismic deformation prediction in the context of geological carbon trapping and storage. Geological Storage of CO2–Long Term Security Aspects 97–113. Springer.
Lecomte, I., 2008. Resolution and illumination analyses in PSDM: a ray-based approach. Lead. Edge 27, 650–663. https://doi.org/10.1190/1.2919584.
Lecomte, I., Lavadera, P.L., Anell, I., Buckley, S.J., Schmid, D.W., Heeremans, M., 2015. Ray-based seismic modeling of geologic models: understanding and analyzing seismic images efficiently. Interpretation-A Journal of Subsurface Characterization 3, Sac71–Sac89. https://doi.org/10.1190/INT-2015-0061.1.
Lecomte, I., Lavadera, P.L., Botter, C., Anell, I., Buckley, S.J., Eide, C.H., Grippa, A., Mascolo, V., Kjoberg, S., 2016. 2 (3) D convolution modelling of complex geological targets beyond–1D convolution. First Break 34, 99–107. https://doi.org/10.3997/1365-2397.34.5.84451.
Li, H., Yang, W., Yong, X., 2018. Deep Learning for Ground-Roll Noise Attenuation, SEG Technical Program Expanded Abstracts 2018. Society of Exploration Geophysicists, pp. 1981–1985.
Lubrano-Lavadera, P., Senger, K., Lecomte, I., Mulrooney, M.J., Kühn, D., 2018. Seismic modelling of metre-scale normal faults at a reservoir-cap rock interface in Central Spitsbergen, Svalbard: implications for CO2 storage. Norw. J. Geol. 99, 329–347. https://doi.org/10.17850/njg003.
Magee, C., Maharaj, S.M., Wrona, T., Jackson, C.A.-L., 2015. Controls on the expression of igneous intrusions in seismic reflection data. Geosphere 11, 1024–1041. https://doi.org/10.1130/GES01150.1.
Michie, E.A.H., Haines, T.J., Healy, D., Neilson, J.E., Timms, N.E., Wibberley, C.A.J., 2014. Influence of carbonate facies on fault zone architecture. J. Struct. Geol. 65, 82–99. https://doi.org/10.1016/j.jsg.2014.04.007.
Mitchell, T., Faulkner, D., 2012. Towards quantifying the matrix permeability of fault damage zones in low porosity rocks. Earth Planet Sci. Lett. 339, 24–31. https://doi.org/10.1016/j.epsl.2012.05.014.
Moussa, M.M., El Arabi, A.G.M., 2003. Soil radon survey for tracing active fault: a case study along Qena-Safaga road, Eastern Desert, Egypt. Radiat. Meas. 37, 211–216. https://doi.org/10.1016/S1350-4487(03)00039-8.
Nixon, C.W., Nærland, K., Rotevatn, A., Dimmen, V., Sanderson, D.J., Kristensen, T.B., 2020. Connectivity and network development of carbonate-hosted fault damage zones from western Malta. J. Struct. Geol. 141, 104212 https://doi.org/10.1016/j.jsg.2020.104212.
Osagiede, E.E., Duffy, O.B., Jackson, C.A.-L., Wrona, T., 2014. Quantifying the growth history of seismically imaged normal faults. J. Struct. Geol. 66, 382–399. https://doi.org/10.1016/j.jsg.2014.05.021.
Pedley, H., House, M., Waugh, B., 1976. The geology of Malta and Gozo. Proc. Geologists' Assoc. 87, 325–341. https://doi.org/10.1016/S0016-7878(76)80005-3.
Pickett, G.R., 1963. Acoustic character logs and their applications in formation evaluation. J. Petrol. Technol. 15 (6), 659–667. https://doi.org/10.2118/452-PA.
Putz-Perrier, M.W., Sanderson, D.J., 2010. Distribution of faults and extensional strain in fractured carbonates of the North Malta Graben. AAPG Bull. 94, 435–456. https://doi.org/10.1306/08260909063.
Rabbel, O., Galland, O., Mair, K., Lecomte, I., Senger, K., Spacapan, J.B., Manceda, R., 2018. From field analogues to realistic seismic modelling: a case study of an oil-producing andesitic sill complex in the Neuquén Basin, Argentina. J. Geol. Soc. 175, 580–593. https://doi.org/10.1144/jgs2017-11.
Renshaw, C., Park, J., 1997. Effect of mechanical interactions on the scaling of fracture length and aperture. Nature 386, 482–484. https://doi.org/10.1038/386482a0.
Rost, S., Thomas, C., 2009. Improving seismic resolution through array processing techniques. Surv. Geophys. 30, 271–299. https://doi.org/10.1007/s10712-009-9070-6.
Rotevatn, A., Fossen, H., 2011. Simulating the effect of subseismic fault tails and process zones in a siliciclastic reservoir analogue: implications for aquifer support and trap definition. Mar. Petrol. Geol. 28, 1648–1662. https://doi.org/10.1016/j.marpetgeo.2011.07.005.
Ryan, H., 1994. Ricker, Ormsby, Klauder, Butterworth - A Choice of Wavelets. CSEG Recorder, pp. 8–9.
Sanderson, D.J., Nixon, C.W., 2018. Topology, connectivity and percolation in fracture networks. J. Struct. Geol. 115, 167–177. https://doi.org/10.1016/j.jsg.2018.07.011.
Schmelzbach, C., Greenhalgh, S., Reiser, F., Girard, J.-F., Bretaudeau, F., Capar, L., Bitri, A., 2016. Advanced seismic processing/imaging techniques and their potential for geothermal exploration. Interpretation 4, SR1–SR18. https://doi.org/10.1190/INT-2016-0017.1.
Schneider, W.A., 1971. Developments in seismic data processing and analysis (1968–1970). Geophysics 36, 1043–1073. https://doi.org/10.1190/1.1440232.
Shipton, Z.K., Evans, J.P., Dockrill, B., Heath, J., Williams, A., Kirchner, D., Kolesar, P.T., Thomas, D., Benson, S., 2005. Natural leaking CO2-charged systems as analogs for failed geologic storage reservoirs. Carbon dioxide capture for storage in deep geologic formations 699–712.
Shipton, Z.K., Evans, J.P., Robeson, K.R., Forster, C.B., Snelgrove, S., 2002. Structural heterogeneity and permeability in faulted eolian sandstone: implications for subsurface modeling of faults. AAPG Bull. 86, 863–883. https://doi.org/10.1306/61EEDBC0-173E-11D7-8645000102C1865D.
Simm, R., Bacon, M., 2014. Seismic Amplitude: an Interpreter's Handbook. Cambridge University Press.
Stewart, S., 2011. Vertical exaggeration of reflection seismic data in geoscience publications 2006–2010. Mar. Petrol. Geol. 28, 959–965. https://doi.org/10.1016/j.marpetgeo.2010.10.003.
Stewart, S., 2012. Interpretation validation on vertically exaggerated reflection seismic sections. J. Struct. Geol. 41, 38–46. https://doi.org/10.1016/j.jsg.2012.02.021.
Talwani, P., 1999. Fault geometry and earthquakes in continental interiors. Tectonophysics 305, 371–379. https://doi.org/10.1016/S0040-1951(99)00024-4.
Vermilye, J.M., Scholz, C.H., 1995. Relation between vein length and aperture. J. Struct. Geol. 17, 423–434. https://doi.org/10.1016/0191-8141(94)00058-8.
Walsh, J., Watterson, J., Heath, A., Gillespie, P., Childs, C., 1998. Assessment of the effects of sub-seismic faults on bulk permeabilities of reservoir sequences. Geological Society, London, Special Publications 127, 99–114. https://doi.org/10.1144/GSL.SP.1998.127.01.0.
Walsh, J., Watterson, J., Yielding, G., 1991. The importance of small-scale faulting in regional extension. Nature 351, 391–393. https://doi.org/10.1038/351391a0.
Wang, Y., 2015. Generalized seismic wavelets. Geophys. J. Int. 203 (2), 1172–1178. https://doi.org/10.1093/gji/ggv346.
Wrona, T., Fossen, H., Lecomte, I., Eide, C.H., Gawthorpe, R., 2020. Seismic expression of shear zones: insights from 2-D point-spread-function based convolution modelling. Journal of Structural Geology 140, 104121. https://doi.org/10.1016/j.jsg.2020.104121.
Yoshida, H., Metcalfe, R., Yamamoto, K., Murakami, Y., Hoshii, D., Kanekiyo, A., Naganuma, T., Hayashi, T., 2008. Redox front formation in an uplifting sedimentary rock sequence: an analogue for redox-controlling processes in the geosphere around deep geological repositories for radioactive waste. Appl. Geochem. 23 (8), 2364–2381. https://doi.org/10.1016/j.apgeochem.2008.03.015.
Zhong, T., Li, Y., Wu, N., Nie, P., Yang, B., 2015. Statistical properties of the random noise in seismic data. J. Appl. Geophys. 118, 84–91. https://doi.org/10.1016/j.jappgeo.2015.04.011.